A Biomechanically and Anatomically Realistic Foot Model (BAREFOOT)

Luke Johnson

A thesis

submitted in partial fulfillment of the

requirements for the degree of

Master of Science in Mechanical Engineering

University of Washington

2018

Reading Committee:

Patrick Aubin, Co-Chair

Eric Rombokas, Co-Chair

Alberto Aliseda

Duane Storti

Pierre Mourad

Program Authorized to Offer Degree:

Mechanical Engineering

University of Washington

Abstract

A Biomechanically and Anatomically Realistic Foot Model (BAREFOOT)

Luke Johnson

Co-Chairs of the Supervisory Committee:
Patrick Aubin, Ph.D.
Affiliate Assistant Professor
Mechanical Engineering

Eric Rombokas, Ph.D.
Affiliate Assistant Professor
Mechanical Engineering

Traditionally, investigators utilize human studies, cadaver studies, and finite element model studies to conduct lower limb biomechanical research. In other realms of biomechanics, a fourth alternative has been recently introduced; strides have been made recently regarding realistic physical model-based studies in place of conventional *in vivo* and *in vitro* study environments. The work presented here includes the development and validation of a biomechanically and anatomically realistic foot (BAREFOOT) 3D printed model. A realistic printed bony geometry and independently validated, elastically realistic printed soft tissue material are developed as subsystems of the BAREFOOT model. As a

stepping stone to a full foot BAREFOOT model, a segmented first-ray model is developed and evaluated. Finally, a full foot BAREFOOT model is developed, printed, and evaluated on a robotic gait simulator (RGS). The RGS results show realistic joint angles and realistic center of pressure trajectory throughout stance phase. The results indicate the utility of the BAREFOOT model in future orthopedic studies and its effectiveness as a study tool.

TABLE OF CONTENTS

LIST OF FIGURES

LIST OF TABLES

ACKNOWLEDGEMENTS

This research was supported by the CDMRP DMRDP Neuromusculoskeletal Injuries Research Award W81XWH-15-1-0417 and Department of Veterans Affairs, Rehabilitation Research and Development Service Grants A9243C, RX002357, and RX002130.

Chapter 1. INTRODUCTION

1.1 MOTIVATION

There are several models traditionally used to study biomechanics, with respective advantages and disadvantages. Human studies, while inherently being the most realistic, are limited by ethical considerations that constrain the types of studies that can be conducted [1]. Cadaveric studies, widen the scope of available experiments that would otherwise be impossible *in vivo*, but have other challenges including: 1) difficulty in procuring specimens with the desired pathologies, 2) difficulty in appropriately altering normal specimens to simulate pathology, and 3) surgeries with cadavers are often destructive and irreversible [2], [3]. A cadaver also has no mechanism to simulate healing [4]. Venturing outside the realm of physical models, there are also computer models at the researcher's disposal. Simulations employing the finite element method (FE) can overcome most of these challenges, but are reliant on accurate assumptions, initial conditions, and must be of sufficient complexity [5]. FE simulations generally require *in vivo* or *in vitro* validation.

More recently, biomechanists have utilized a fourth alternative, physical model-based biomechanical testbeds. Most significant and closely aligned with the work presented here, of these physical models, is the anatomically-correct testbed (ACT) hand. The ACT hand mimics the active and passive dynamics of a human hand and serves as an experimental testbed to investigate neural control of hand movements [6]. This model was used to explore the human hand's utilization of muscle synergies when transitioning between different force-stiffness conditions [7]. Additionally, path integral reinforcement learning was applied to the ACT hand's musculotendon network to manipulate a light switch, finding, among other things, that the hand learned to rely on flexors more than extensors to minimize an energy cost function [8]. The work presented here seeks to

achieve a similarly useful physical model to ask biomechanical questions, albeit in this case a foot model.

1.2 DEFINING BAREFOOT

Here I present my work towards the creation and validation of a 3D printed, **B**iomechanically and **A**natomically **Re**alistic **FOOT** model (BAREFOOT). Using a 3D printer, I aim to print out testbed foot models for use in biomechanical and orthopedic research. These would negate many of the disadvantages found in other methods. Patient-specific geometries can be scanned then printed, and the model can replicate many scannable pathologies found in humans. Sensors can be integrated into the print, allowing sensor placement that would otherwise be highly invasive. Multiple copies of the exact same model can be printed, allowing for intra-patient comparisons even in the presence of destructive testing. The models are subject to the laws of physics; friction, contact mechanics, and other phenomena don't need to be numerically simulated. Lastly, bone healing can be simulated in these models by altering the geometry in a CAD environment prior to printing. Computer simulations have made a major impact in how science is conducted, and I anticipate that physical, realistic biomechanical testbeds will similarly open new avenues of exploration that would have been impossible otherwise.

The foot used to create the BAREFOOT model presented here is a right foot, the geometry of which is sourced from the CT scan of a healthy, middle-aged male. Throughout the course of my master's thesis, models of varying complexity have been developed. Initial models only included the first ray and were used to study the first metatarsophalangeal (MTP) joint. As the work progressed, additional features were added into the foot model to improve the realism, and eventually a full foot model was produced and tested. All printed foot models underwent some form of validation which varied from model to model.

1.3 SCOPE OF BAREFOOT

The very first working BAREFOOT model only included the first ray and used solid material infills. This model featured a plantar aponeurosis to transmit force to the proximal phalanx of the first ray, and had a slot cut superior to the first MTP such that an intrajoint pressure sensor could be installed. This model was validated via plantar pressure and intrajoint pressure measurements. The plantar pressure measurements motivated the next phase of my thesis work, which was creating lattice microstructures to lower the Young's modulus of the softest printable material, such that it would distribute force similarly to fat. The next BAREFOOT model was the same first ray model as before, but the material representing fat consisted of simple cubic lattice microstructures rather than a solid infill as before. This yielded better plantar pressure measurements but proved to be very weak and failed early on in testing, even at ¼ bodyweight (BW).

The next iteration of BAREFOOT was still a first ray model but has some substantial differences regarding biomechanical realism. The lattice microstructure was entirely reworked from simple cubic to gyroid, which still achieved a similar elastic profile to fat but was far stronger and resistant to fatigue. Additionally, biomechanically accurate but not anatomically accurate ligaments were incorporated that realistically limited the range of motion (ROM) of the first ray MTP. To build in these ligaments, the slot for the joint pressure sensor was removed. Instead of joint pressure, plantar pressure would be the only source of validation for this model. Finally, the tendon routing was modified to follow the line of action of the flexor hallucis longus rather than the plantar aponeurosis.

The subsequent final working model expanded upon the success of the previous first ray design, and all five rays were included. Because of space requirements, only the first ray had a

biomimetic MTP joint and the other four had reasonable stiffness, but no regards were given to ROM. Four new flexor digitorum longus tendons were added in addition to the existing flexor hallucis longus. Although the four added flexors join into a single tendon in the midfoot anatomically, they were routed around the calcaneus and up the tibia so the force on each could be varied independently. The tendon routing was performed in this manner to avoid having to tie together tendons internally post-print, and as a precaution against slightly incorrect tendon lengths and thus moment arm lengths. The full foot model also had marker sticks pointing out of the y-axes of all bones in the first ray to add relative bone motion as a validation step, in addition to the existing plantar pressure pipeline.

Chapter 2. 3D PRINTED LATTICE MICROSTRUCTURES

2.1 MOTIVATION FOR LATTICE MICROSTRUCTURES

One of the principal mechanical quantities of biomechanical models is the modulus of elasticity, or Young's modulus (E). Tissue compression, governed by Young's modulus E, plays a significant role in the distribution of external forces to the bones and thus affects intra-joint contact pressure. Currently, Young's modulus can be tuned by casting various rubber mixes and gels [9]–[11], a labor-intensive and multi-step process. Furthermore, casting isn't possible for all geometries. Another method involves cyclically freezing and thawing a polyvinyl alcohol-based cyrogel [12], which requires special tools and appliances, and again is labor intensive. However, recent advancements in 3D printing open a new avenue for the creation of artificial biological materials. Polyjet printers can produce a variety of different materials contained within the same print, some of which have elastic properties close to those of ligaments and bones [13]. Materials capable of mimicking the properties of very soft tissues like plantar fat (e.g. the fat pad under the foot) are not yet available, and are often cited as a barrier for using 3D printers to create parts with the desired elastic properties [10], [14], [15].

This shortcoming may be partially addressed using techniques pioneered in research into mechanical metamaterials - artificial materials whose mechanical properties are dictated by their structure in addition to, or in spite of, their bulk composition [16]–[18]. Metamaterials typically are constructed to exhibit properties that are otherwise impossible to find in nature, but here we use microstructures – lattices incorporating voids in the bulk material – to increase the compliance of the materials available for 3D printing. By varying the micro-scale structure of how the material is deposited, we can vary the macro-scale elastic properties of the object. The advantages of using

3D printed metamaterials to mimic mechanical properties have been recently realized for mimicking aortic tissue in a valve implant efficacy study [19]–[22].

2.2 Cubic Lattice Microstructures Definition

The first type of lattice microstructure I explored was a simple cubic lattice. A simple cubic lattice implies a cubic lattice cell with lattice points at all 8 corners of the unit cell and all three interaxial angles equal to 90 degrees (figure 2.1). This type of lattice was chosen initially for simplicity, as software already in our current mesh pipeline (Autodesk Meshmixer) had cubic lattice generation as a built-in feature.

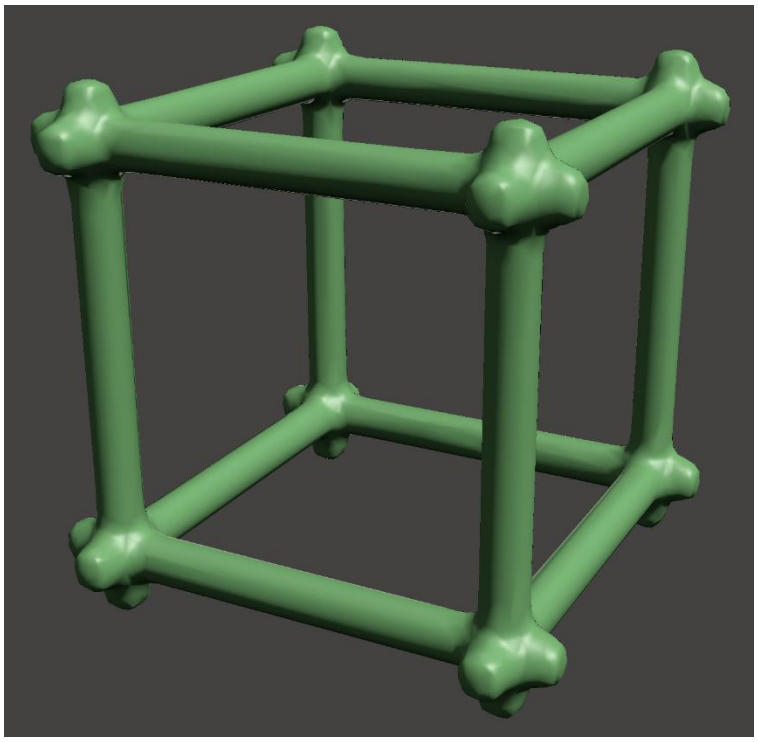

Figure 2.1. Simple cubic lattice unit cell.

2.3 Cubic Lattice Methods

Five variables were modified to create different lattices: element diameter, element spacing, element cross-sectional geometry, element arrangement, and lattice rotation (figure 2.2). Element diameter (ED) refers to the diameter of the cylindrical elements. Element spacing (ES) refers to the distance between repeated element centroids. Element cross-sectional geometry refers to the 2-dimensional shape of the element, e.g. circular, square, or triangular. The sizes of the non-circular elements are chosen to keep element cross sectional area constant with respect to the best-fit lattice. Element arrangement refers to the pattern by which repeated elements are laid out, e.g. square, hexagonal, or triangular patterns. Lattice rotation refers to an x-axis rotation of the whole lattice with respect to the printer's and material tester's vertical z-axis. A lattice rotation of 0° means the vertical columns of the lattice are aligned with the printer's and material tester's vertical z-axis, a rotation of 10° means the vertical columns of the lattice are 10° askew from the printer's and material tester's z-axis (figure 2.2(A)). For each variable, 3-5 samples were created with incremental changes in the variable, while the four other variables were held constant. This allowed for a change in one variable to be observed in isolation.

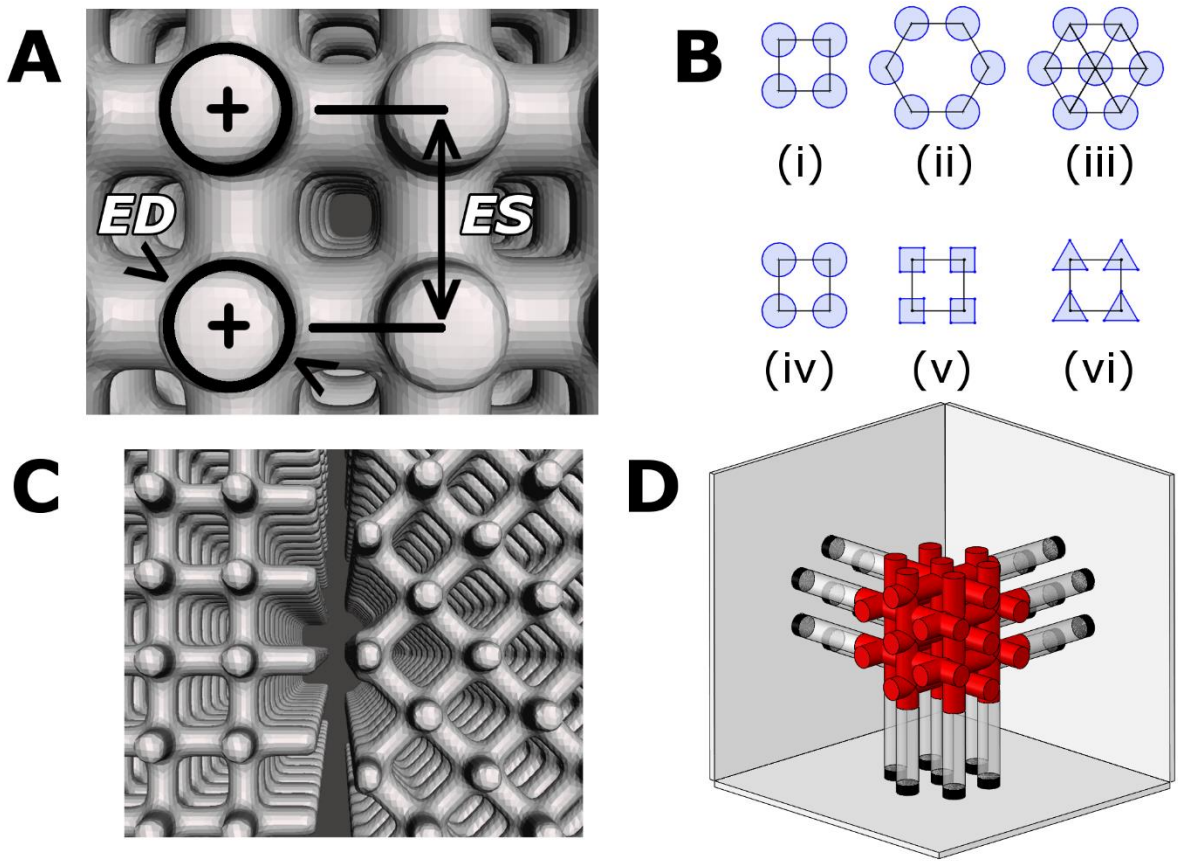

Figure 2.2. (A) Diagram showing the lattice variables element diameter (ED) and element spacing (ES). (B) Top row is cross-sectional view of lattice when varying element arrangement, bottom row is that when varying cross-sectional geometry: (i) Square arrangement. (ii) Hexagonal arrangement. (iii) Triangular arrangement. (iv) Circular geometry. (v) Square geometry. (vi) Triangular geometry. (C) Image of non-rotated lattice (left) and lattice rotated to 45° (right). (D) A CAD visualization of how a unit cell is constructed. The cross-sections shown in (B) are extruded from each principal plane to form a unit cell. This particular unit cell is that formed from B-iii.

There were two distinct pipelines for generation of lattice samples. At the beginning of both workflows, a cylinder with a diameter of 19 mm and height of 11 mm was generated in Solidworks (Dassault Systemes). This 19x11 mm cylinder acted as the bounding volume for all subsequently generated lattices. The dimensions were chosen to mimic cadaveric fat samples used in a previous study [23].

2.3.1 *Meshmixer Pipeline*

For the majority of generated lattice samples, the previously generated cylinder in Solidworks was exported as an STL file and then imported into Meshmixer (Autodesk). In Meshmixer, a lattice was generated, bounded by the cylinder, using the Pattern feature. The mesh file for the cylinder was then discarded and the resulting lattice was exported as an STL file. Meshmixer's pattern feature only allowed for square lattices with cylindrical columns, which worked for the majority of samples. Samples varying element diameter, element spacing, and lattice rotation were included in this pipeline.

2.3.2 *Solidworks Pipeline*

Because of the limitations of Meshmixer's Pattern feature, the remaining samples (corresponding to element cross-sectional geometry and element arrangement) required modeling in Solidworks. In copies of the same part file in which the original cylinder was generated, lattice geometries were created, again bounded by the cylinder. This was achieved by creating patterned sketches on the three principal axes and extruding them through to create a body separate from the cylinder. A Boolean intersect operation was then performed between this new body and the original cylinder, yielding the lattice bounded by the cylinder dimensions. The resulting solid body was then exported as an STL file.

2.3.3 *3D Printing*

The 3D printer used to print the generated samples was a Connex3 Objet350 (Stratasys). The STL files containing the lattice samples were imported into the Stratasys print manager for the Connex3 (Objet Studio). They were printed in TangoPlus (FLX930), the softest material available, with dissolvable support material (SUP706). After printing, the samples were submerged in an aqueous

solution with 1% Sodium Metasilicate and 2% Sodium Hydroxide by mass. Agitated with a magnetic stirrer, the support was dissolved out of the samples after 6-10 hours in solution, with the solution swapped every 2-3 hours. After full dissolution of the support material, the samples were rinsed in water, then placed in small, airtight containers. These containers were placed in a dark drawer for two days before material testing.

2.3.4 *Cubic Lattice Material Testing*

The printed samples were tested on a Bose 3200 material testing system. The same compression testing protocol was used as in Dr. Pai's cadaveric study which characterized plantar fat [23] to ensure quantitatively comparable results. The samples were subjected to triangle waves, at 1 Hz frequency, with magnitude such that the sample was compressed to a maximum of 54% strain. Each sample was tested for 15 cycles, with the first 14 cycles acting as a method of conditioning the material. For all tests, the z-axis of the sample, defined as the z-axis of the 3D printer, was aligned with the compression z-axis of the material testing system.

Calibration was performed using WinTest's (Bose) TuneIQ tool for each sample. The force/displacement data from the Bose machine was exported as a CSV file for importation into MATLAB (The MathWorks, Inc., Natick, MA). For each sample, the cross-sectional area was considered the same at 283.5 mm^2 (area of 19.00 mm circle). The initial height of each sample was calculated according to a 0.10 N preload, per Pai's study [23].

2.3.5 *Analysis*

The CSV files from WinTest were imported into MATLAB. From the force/displacement data, stress-strain values were calculated for all cycles, via the following equations.

$$\sigma = \frac{F}{A_o} \tag{2.1}$$

$$\varepsilon = \frac{L - L_o}{L_o} \tag{2.2}$$

In (2.1), σ is engineering stress, F is force from the machine, and A_o is the initial cross-sectional area of each sample. In (2.2), ε is strain, L is sample height derived from the machine and L_o is the initial sample height. After these equations were applied to the data to find stress and strain as a function of time for each sample, the results were plotted in MATLAB for the final two full displacement cycles. Additionally, the elastic modulus was determined at 10%, 30%, and 50% on the resulting stress-strain curve for each sample according to the following equation.

$$E = \frac{\sigma}{\varepsilon} \tag{2.3}$$

In (2.3), E is the elastic modulus, σ is engineering stress from (2.1), and ε is strain from (2.2). Because the stress-strain plots for the samples were highly non-linear, a single elastic modulus wasn't sufficient to describe the elastic properties of the material. Instead, three elastic moduli were computed for each sample during the final load cycle, at 10%, 30%, and 50% strain.

2.4 Cubic Lattice Results

Fourteen samples with different geometries were tested. We studied the effect of varying five lattice properties (element spacing, cross-sectional geometry, diameter, cross-sectional area, lattice rotation, and element arrangement) from the baseline lattice (S1) by measuring the samples' elastic moduli at 10, 30 and 50 percent strain (tables 2.1-2.5). All the samples demonstrated a non-linear stress-strain curve that absorbed energy when loaded (figure 2.3). Varying lattice rotation, while holding all others constant, had a pronounced effect on the non-linearity and energy absorption of the sample (figure 2.4(D)).

The range of elastic moduli we were able to achieve at 10, 30 and 50 percent strain varied from 2.36, 2.37 and 202 kPa (softest) to 2440, 2550 and N/A[1] kPa (hardest), respectively, a range of three orders of magnitude. The softest sample (S4) was a square lattice with cylindrical columns of 0.5 mm diameter and 1.2 mm spacing, rotated to $\theta = 11^0$. The hardest sample was simply a solid plug of printed TangoPlus (FLX930) material (S14).

The sample that most closely resembled cadaveric plantar fat (S1) had an elastic modulus of 7.55, 9.50 and 252 kPa at 10, 30 and 50 percent strain, respectively. This best-fit lattice (S1) was a simple cubic lattice with cylindrical columns of 0.5 mm diameter and 1.2 mm spacing without any rotation. A simple cubic lattice implies a cubic lattice cell with lattice points at all 8 corners of the unit cell and all three interaxial angles equal to 90 degrees.

Changing the element diameter and element spacing variables had the largest effect on the resulting elastic profile (figure 2.4(A), (C)). Shifting the element diameter from 0.5 to 0.7 mm changed the Young's moduli from 7.55, 9.50 and 252 kPa to 173, 148 and 1020 kPa at 10, 30 and 50 percent strain, respectively (table 2.1). Altering the element spacing from 1.2 to 1.0 mm changed the Young's moduli from 7.55, 9.50 and 252 kPa to 2.56, 48.4 and 693 kPa respectively, at the same strain values (table 2.2).

Element cross-sectional geometry and element arrangement had little effect on the resulting stress-strain curve (figure 2.4(B), (E)). Circular and square cross-sectional geometries had Young's moduli of 7.55, 9.50 and 252 kPa and 9.04, 17.1 and 267 kPa at 10, 30 and 50 percent strain, respectively (table 2.3), and square and hexagonal element arrangements had Young's moduli of 7.55, 9.50 and 252 kPa and 11.6, 29.9 and 289 kPa at 10, 30 and 50 percent strain, respectively (table 2.4). Lattice rotation tended to linearize the elastic profile. For example, a 45°

[1] Straining the solid sample (S14) past 30% generated forces outside of load cell's range.

lattice rotation yielded Young's moduli of 16.0, 12.1 and 29.9 kPa at 10, 30 and 50 percent strain, respectively (table 2.5).

Table 2.1. Effect on Young's modulus by varying element diameter from that of baseline

Diameter	0.5 mm (S1)	0.7 mm (S2)	0.9 mm (S3)	Solid (S14)
E (kPa) @ 10% ε	7.55	173	565	2440
E (kPa) @ 30% ε	9.50	148	919	2550
E (kPa) @ 50% ε	252	1020	1500	N/A[2]

Table 2.2. Effect on Young's modulus by varying element spacing from that of baseline lattice (S1).

Spacing	1.2 mm (S1)	1.0 mm (S9)	0.8 mm (S8)	Solid (S14)
E (kPa) @ 10% ε	7.55	2.56	10.7	2440
E (kPa) @ 30% ε	9.50	48.4	334	2550
E (kPa) @ 50% ε	252	693	1020	N/A[2]

Table 2.3. Effect on Young's modulus by varying cross-sectional geometry from that of baseline lattice (S1).

C-S Geometry	Circular (S1)	Square (S11)	Triangular (S10)
E (kPa) @ 10% ε	7.55	9.04	20.7
E (kPa) @ 30% ε	9.50	17.1	23.9
E (kPa) @ 50% ε	252	267	356

Table 2.4. Effect on Young's modulus by varying element arrangement from that of baseline lattice (S1).

Arrangement	Square (S1)	Hexagonal (S12)	Triangular (S13)
E (kPa) @ 10% ε	7.55	11.6	10.9
E (kPa) @ 30% ε	9.50	29.9	25.7
E (kPa) @ 50% ε	252	288.9	274

Table 2.5. Effect on Young's modulus by varying lattice rotation from that of baseline lattice (S1).

Rotation	0° (S1)	11° (S4)	22° (S5)	33° (S6)	45° (S7)
E (kPa) @ 10% ε	7.55	0.912	N/A[3]	12.1	16.0
E (kPa) @ 30% ε	9.50	3.70	10.8	8.87	12.1
E (kPa) @ 50% ε	252	268	175	35.2	29.9

[2] Straining the solid sample (S14) past 30% generated forces outside of load cell's range.
[3] S5 was so soft that the .2N preload strained the sample beyond 10%.

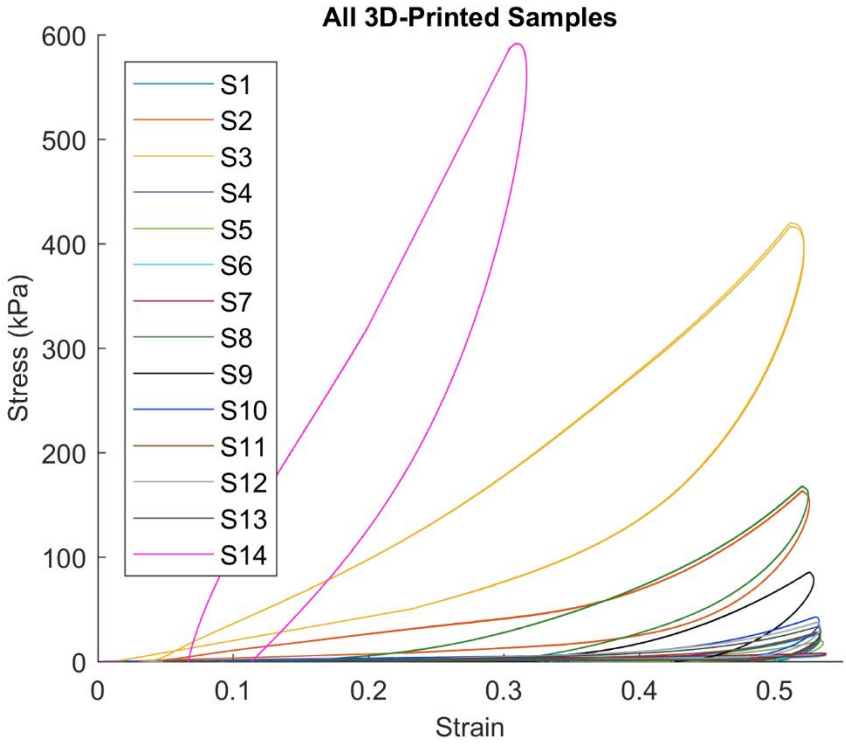

Figure 2.3. Stress (kPa) vs. strain plot for all printed samples, including the non-latticed, solid sample (S14).

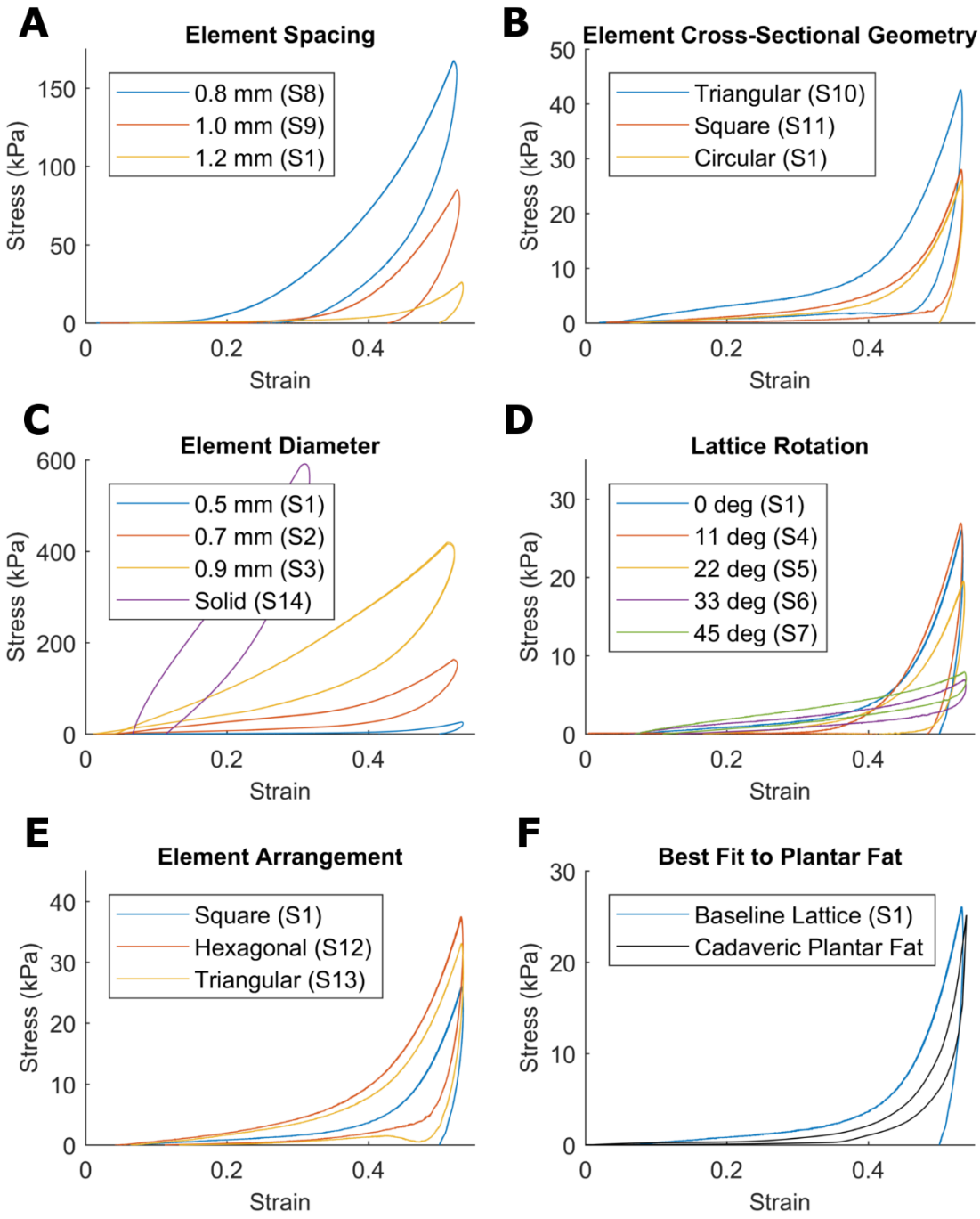

Figure 2.4. Array of stress (kPa) vs. strain plots for all printed samples included in the study. (A) Samples with variable element spacing. (B) Samples with variable cross-sectional geometry. (C) Samples with variable element diameter. (D) Samples with variable lattice rotation. (E) Samples with variable element arrangement. (F) The lattice sample (S1) that most closely matched cadaveric plantar fat.

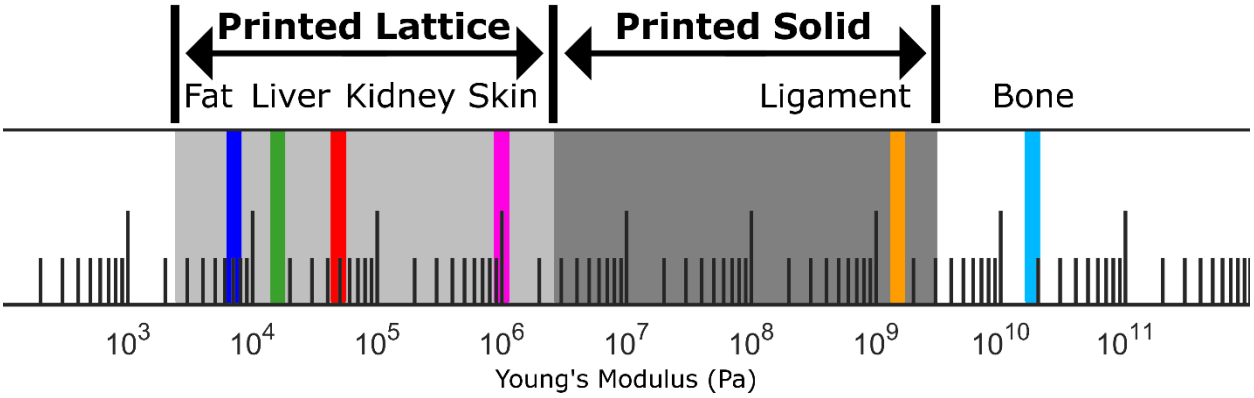

Figure 2.5. Average Young's moduli for various biological materials [24], [25] including both hard and soft tissues, are displayed on a logarithmic scale. Underlain are the range of moduli available through our printed lattice microstructures and that from solid prints of PolyJet material [13].

2.5 Cubic Lattice Discussion

We have identified five lattice parameters and quantified their effect on stress-strain properties. Element diameter and element spacing had the largest effect on the Young's modulus and linearity of the elastic profile of the samples (figure 2.4). Element cross-sectional geometry had a relatively negligible effect on the Young's modulus, likely due to element cross-sectional area being held constant. Similarly, element arrangement had little effect on Young's modulus, as the column density was held constant despite the differing geometric arrangements. Lattice rotation is an excellent tool to change the linearity of the elastic curve.

We found a lattice structure that, to a large extent, matched the properties of plantar fat. This lattice reduced the elastic moduli at 30 percent strain from 2,550 kPa for the bulk "soft" tango material to just 9.50 kPa. The elastic moduli of real plantar fat at 10, 30 and 50 percent strain was previously reported as 1.08, 7.13, and 188 kPa [23], which is quantitatively very close to that of this lattice. Qualitatively the samples stress-strain curve also compares well to cadaveric fat (figure

2.4(F)). These results show that latticing can expand the range of 3D-printed material properties to include plantar fat and other biological soft tissues (figure 2.5).

Compared to plantar fat, the best-fit lattice sample S1 had a toe region at a slightly lower strain value and exhibited greater hysteresis. The discrepancies between the elastic moduli of real fat and our best-fit lattice (S1) can be explained largely by the different damping properties of the 3D-printed material and actual fat. Both the 3D-printed and cadaveric fat samples were tested with 1 Hz triangle waves. The area between the load and unload curves (figure 2.4(F)) is representative of energy loss and positively correlated to a material's coefficient of damping [24]. Due to the hysteresis present, we expect an improved fit at lower cycle rates. Also note that, based on the effects of element diameter and element spacing (figure 2.4(A), (C)), it appears that lower diameters and larger spacings move the toe region to higher strain values and yield a better fit. Samples with smaller diameters and larger spacings were fabricated, but were too fragile for support material dissolution and so were not tested. The fragility of these samples was most prominent in the printer's Z plane, resulting in the samples coming apart as intact layers.

Worth noting are similar efforts from other groups toward the goal of tuning the elastic modulus of 3D printed materials through the creation of lattice microstructures. Prior work involves the development of software to automatically generate lattice structures in a mesh file, using the color properties of the mesh to denote a range of Young's moduli according to a defined mapping array [25]. Based on the color value of each triangle, specific lattice properties were generated such that the elasticity in that specific region was correct according to the color to Young's modulus mapping. Limitations of this work, as cited by the authors, are that it can only generate accurate Young's moduli at small strain values, and only works for linearly elastic

materials. While this technique has many potential applications, most biomechanical tissue simulation applications require nonlinear elasticity.

Another group recently applied 3D printed metamaterials to mimic aortic tissue [19]. The motivation for their work was largely similar to ours, that being the stress-strain curves of commercially available photopolymers is a significant barrier to realistic physical models [21]. They were also likewise critical of numerical simulation and saw their 3D-printed phantom as a superior alternative for simulation. The specifics of this group's metamaterials differ substantially from those of ours in that they combined materials to achieve specific stress-strain properties, as opposed to creating lattice geometries of one material to go softer than is commercially available through material combinations [19]–[22]. Despite methodical differences, the success of their similarly-motivated study further reinforces the efficacy of the work presented here.

One limitation of the technique we describe here is that it requires a great deal of human labor. Automation of the lattice generation workflow would be required to make this practical for complex, system-scale testbeds like entire limbs. We also expect that Finite Element Analysis (FEA) could complement our technique by predicting the Young's modulus of proposed lattice microstructures before they are fabricated. Given a desired Young's modulus, an inverse-FEA approach could be used to hone in on candidate microstructure parameters before fabrication.

Another limitation of is that we have thus far only considered a single 3D printed material, TangoPlus (FLX930). However, we expect that our results can be generalized to other commercially-available, elastomeric 3D printer materials. There could be advantages in mixing materials in order to avoid fragility across layers, while taking advantage of compliance in other dimensions.

2.6 Gyroid Lattice Microstructure Motivation and Definition

While the cubic lattice microstructures were able to be tuned to closely match cadaveric plantar fat, the cubic lattice didn't sustain full body weight loading (section 3.2). To produce a BAREFOOT model that has soft tissue that mimics biological tissue but is also strong enough to withstand full body weight, it was decided that we pursue an entirely different kind of lattice microstructure, one with a larger element diameter, minimal stress raisers, and still tunable to match soft tissue. The Schoen gyroid, a triply periodic minimal surface, was chosen for its excellent strength properties [26], [27].

2.7 Gyroid Lattice Methods and Results

Unlike in the cubic lattice study, the gyroid lattice only had two parameters that define its shape and thus macro lattice stiffness: volume percent and unit cell size. These were analogous to element diameter and element spacing, respectively, in the cubic lattice study. The volume percent and element diameter analogy isn't one-to-one however, as an effective element diameter with a gyroid is achievable by infinitely many volume percent and unit cell combinations. In other words, a gyroid's element diameter is a function of volume percent and unit cell size, and element spacing is one-to-one and is purely a function of unit cell size.

Using the experience and insight I had gained from the lattice study, I was able to quickly generate a set of structures that I believed would include a lattice that closely matched plantar fat (figure 2.6). The testing protocol used was the same as in the cubic lattice study (section 2.2.4), and indeed one of them was within the margins of the curve profile we were aiming for.

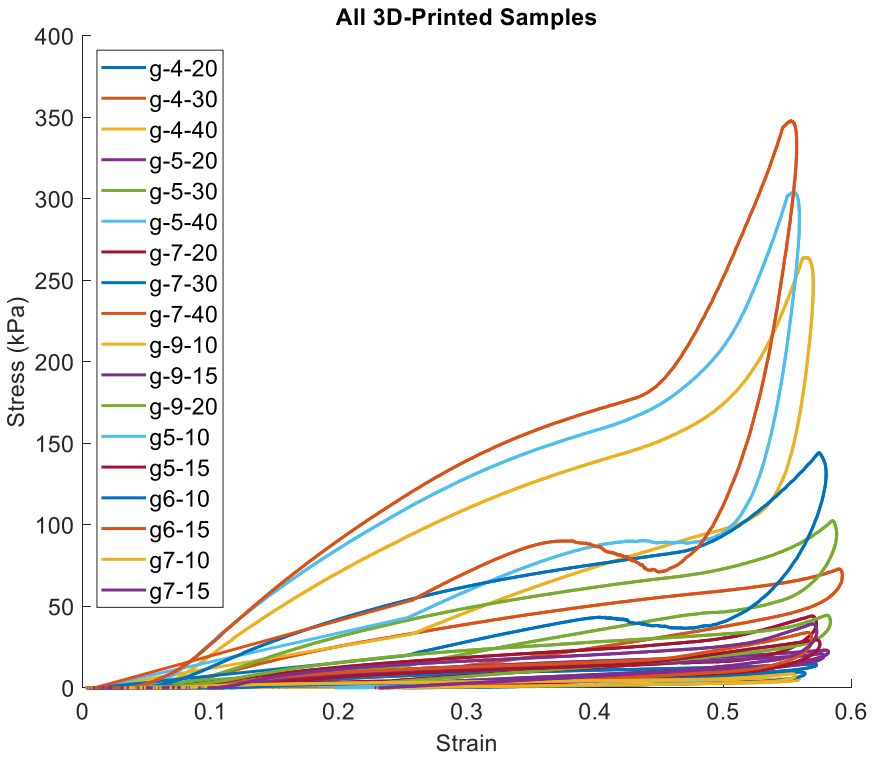

Figure 2.6. Stress-strain curves for all printed gyroidal lattice microstructure samples. As to nomenclature, the "g" stands for "gyroid", the first number is unit cell size (mm), and the second number is volume percent.

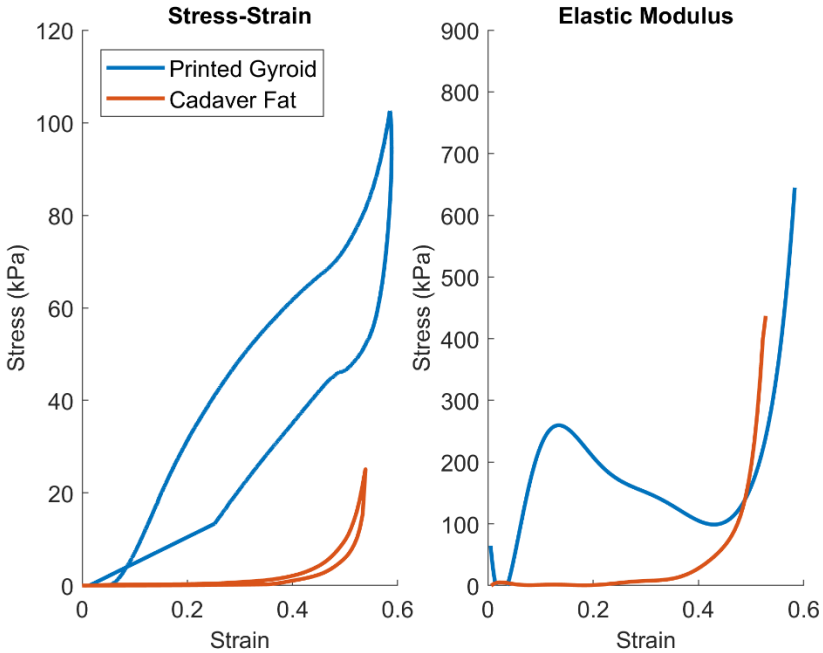

Figure 2.7. (Left) Stress-strain of chosen gyroid. (Right) Elastic modulus of chosen gyroid.

The specific gyroidal lattice microstructure of those evaluated was chosen for the similarities of its elastic profile to that of cadaveric plantar fat. The chosen gyroid had a unit cell size of 5 mm and a 30 percent volumetric fill. While the stress-strain curve for this gyroid was vertically offset from that of plantar fat, the Young's modulus as a function of strain was similar, especially at the toe region (figure 2.7).

Chapter 3. FIRST RAY BAREFOOT MODELS: TOWARDS A FULL FOOT MODEL

As an example of how the BAREFOOT model can be used to improve foot and ankle orthopedic care, here we present a case study using a first ray toe model. To motive this work, we examine Hallux Rigidus, arthritis of the big toe, which has ill-defined best practices for joint preserving surgical treatment options.

3.1 Solid Soft Tissue – Hallux Rigidus Case Study

Hallux Rigidus (HR) is characterized by arthritis of the big toe in the first MTP joint and the accompanying typical symptoms – stiffness, osteophyte growth, etc. We chose to explore the utility of BAREFOOT by recreating the results of a cadaveric study in which a certain surgical procedure to treat HR, known as the Moberg osteotomy, was performed on a cadaver and the MTP joint pressure distribution was measured before and after the procedure [28]. There are a variety of surgeries used to treat HR, and the Moberg is one of them. The Moberg is characterized by osteophyte removal and removing a wedge from the first proximal phalanx (PP), and then refusing the bone to shift the center of pressure (COP) in the plantar direction in the sagittal plane. We performed this surgery in CAD (figure 3.1) and printed the pre- and post-surgery foot, evaluating the joint pressure map in each case.

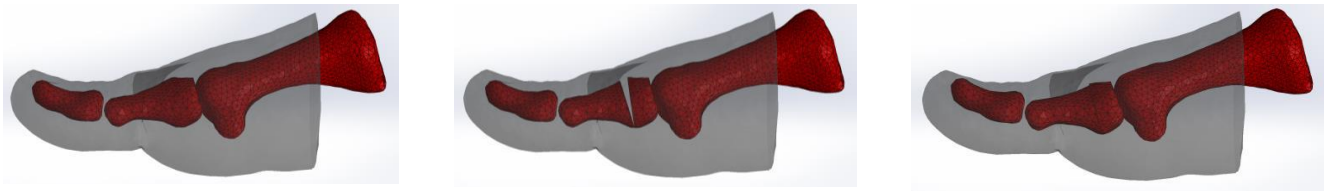

Figure 3.1. (Left): Pre-Moburg cross sectional view of foot geometry. (Center): Osteotomy wedge removed. (Right): Post-Moburg with osteotomy reduced (PP fused).

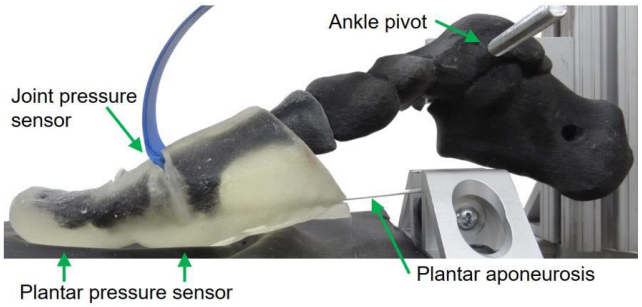

Figure 3.2. Custom loading frame to load the BAREFOOT model in a manner consistent to walking by pulling on the plantar aponeurosis.

A test rig was built that applied known force to a cord attached to the PP, mimicking the plantar aponeurosis tendon (figure 3.2). Joint pressure mappings were measured for the pre- and post-surgery versions of the 3D-printed feet. The results were representative of the desired outcomes of the Moberg osteotomy, a plantar shift in the COP in the MTP joint (figure 3.3). We were successful in our attempts to show the viability of BAREFOOT as a biomechanical testbed. By using the BAREFOOT model to test the results of the other HR surgical treatments, we envision an orthopedic study utilizing BAREFOOT to objectively determine a best surgical option for HR within a certain class of HR pathologies.

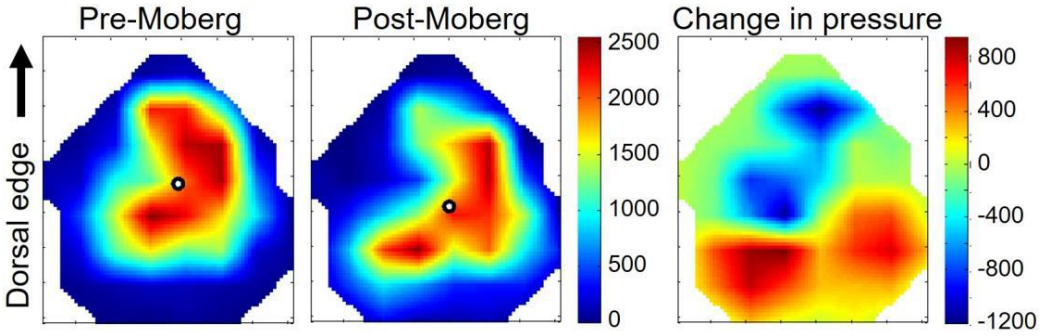

Figure 3.3. Comparison of MTP joint contact pressure (kPa) before (left) and after (center) a Moberg osteotomy. On the right is in image showing the change in pressure pre- and post-surgery, red denoting an increase in pressure and blue a decrease. The COP was shifted in the plantar direction by 0.9 mm.

One major limitation of the case study was that the 3D printer we used (Connex3 Objet 350) couldn't print soft enough to accurately represent soft tissue, visible in the plantar pressure results (figure 3.4). The softest material available, named Tango, was simply too stiff. Additionally, we only modeled the foot with only two different materials, Tango (softest material available) for soft-tissue and Vero (hardest material available) for bone. This was the original inspiration for our investigations into lattice microstructures (section 2).

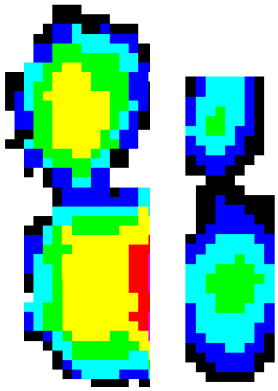

Figure 3.4. (Left) *In vivo* subject data. (Right) BAREFOOT single ray HR model.

3.2 Simple Cubic Lattice Microstructure Soft Tissue

Following the HR study's plantar pressure results (figure 3.4), we applied the best-fit cubic lattice microstructure (sections 2.1. – 2.4.) to the soft tissue regions of the first ray model (figure 3.5). The plantar pressure results improved, but the model was far less durable than the previous version.

Figure 3.5. Cubic lattice applied to first ray BAREFOOT model. Peeling along layers was an issue and was the primary motivation to seek a new lattice type.

The lattice microstructure suffered from delamination before any testing had occurred, during support dissolution due to relative fluid motion in the cleaner bath (figure 3.5). Printed layers tended to delaminate in between nodes, due to a combination of z-axis weakness (inherent to layer-based printing), small element diameter, and large stress raisers at the lattice nodes.

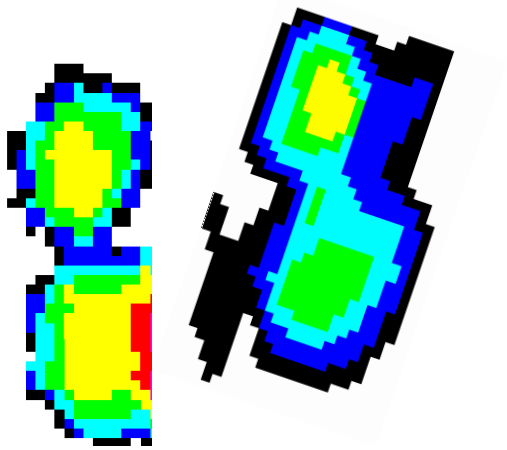

Figure 3.6. (Left) *In vivo* subject data. (Right) BAREFOOT single ray cubic lattice microstructure model. The foot was rotated on the pressure mat during data acquisition, which is why the pixels are diagonal.

The plantar pressure results of the first ray model with cubic lattice soft tissue (figure 3.6) matched more closely to the *in vivo* subject data that that of the first ray model with solid printed material as the soft tissue (figure 3.4). The plantar pressure was more distributed with the cubic lattice microstructure. However, the non-zero pressures to the right of the phalanges were due to delaminated lattice layers shifting over and transmitting force – there were no second ray phalanges that could have been responsible for this. It was decided that a more robust lattice needed to be developed.

3.3 Gyroid Lattice Microstructure First Ray Model

Following failures associated with the simple cubic lattice microstructure applied to the first ray model (section 3.2), the switch was made to gyroid lattice microstructures (sections 2.6, 2.7). This

gyroid lattice microstructure was applied to the same soft tissue regions as in previous models (figure 3.7).

Figure 3.7. First ray BAREFOOT model with gyroid lattice microstructure.

Unlike previous first ray model that were tested on a static load frame, this model was tested on the RGS. As such, ensuring the ground plane was in the correct orientation relative to the BAREFOOT wasn't trivial as in previous trials. The high pressure under the sesamoids in the BAREFOOT model as compared to the subject's *in vivo* data is evidence of error in the applied ground plane rotations.

The coordinate systems used to define the ground plane angle relative to the foot had a large amount of error through arbitrary bony landmark designations, as these landmarks were designated from a 2D image and projected onto a 3D surface [3]. (3.1) - (3.4) were used to generate the talus coordinate system from the landmarks.

$$\overrightarrow{v3} * \overrightarrow{v1} = \vec{x} \tag{3.1}$$

$$\overrightarrow{v3} * \overrightarrow{v2} = \overrightarrow{dummy} \tag{3.2}$$

$$\vec{x} * \overrightarrow{dummy} = \vec{y} \tag{3.3}$$

$$\vec{x} * \vec{y} = \vec{z} \tag{3.4}$$

In (3.1) - (3.4), $\overrightarrow{v1}$ through $\overrightarrow{v3}$ are vectors representing the relative positions of three bony landmarks on the talus [3], $\vec{x}$, $\vec{y}$, and $\vec{z}$ are the three principal axes of the talus, and $\overrightarrow{dummy}$ is a temporary vector.

Rotation issues aside, the resulting pressures were distributed adequately and the durability issues from the previous iteration were completely absent in this model (figure 3.8).

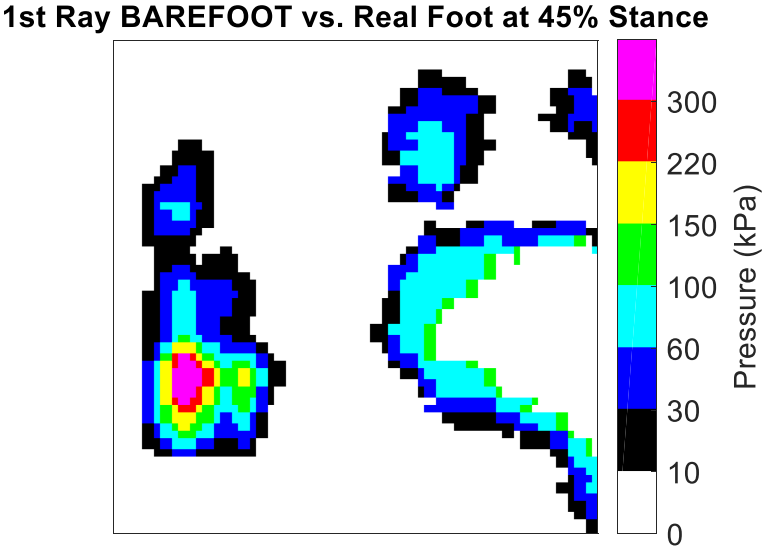

Figure 3.8. First ray gyroidal BAREFOOT results from RGS at 100% BW and 45% stance phase, compared to subject's *in vivo* data at the same pose.

Chapter 4. FULL FOOT BAREFOOT MODEL

4.1 FULL FOOT MOTIVATION

We propose the use of 3D printing in biomechanical physical models to displace more time-consuming and manufacturer-specific methods such as mold-making and casting. 3D printed feet can model many different scannable bony pathologies and are highly dimensionally accurate. Unlike other types of physical models, 3D printed models do not require extensive handwork and rely on the accuracy of the printer rather than the skill of the manufacturer. As such, printed physical models are replicated easily simply by printing the file set again, and can be digitally distributed to others.

Here we present BAREFOOT (Biomechanically and Anatomically REalistic FOOT model), a 3D printed and validated physical foot model for use in biomechanical orthopedic studies. BAREFOOT has two tendons (flexor hallucis longus and flexor digitorum longus) and realistic soft tissue made form a gyroidal lattice microstructure that mimics the elastic properties of cadaveric plantar fat. The purpose of this paper is to explain the methodology behind creating the BAREFOOT model and present validation measures of plantar pressure and bone kinematics collected from "walking" the BAREFOOT model in our robotic gait simulator (RGS) [29].

4.2 FULL FOOT METHODS

4.2.1 *Overview*

Static CT imaging and walking plantar pressure and ground reaction force data was collected from a single subject and used as the source data for the patient-specific BAREFOOT model. The subject's scans were segmented into surface mesh files, and manipulated in CAD to incorporate

tendon routing, ligaments, realistic soft tissue, and various other features. The modified surface meshes were then printed using a multi-material printer, the Objet350 Connex3 (Stratasys, Eden Prairie, MN). After printing, support was dissolved from the foot and the 2 mm polyester tendon cords were installed. The BAREFOOT model was then evaluated on the RGS, comparing, at various stances, plantar pressure results to the subject's *in vivo* data and relative bone motion to cadaveric data [3].

4.2.2 *Subject Specific Input Data*

The subject in this study was a 43-year-old male, 945 N body weight. Procedures were performed with IRB approval and after informed consent [30]. An MRI scan was performed on the subject's right foot using a 3.0T Phillips Achieva MRI spacing at the Bio-Molecular Imaging Center at the University of Washington (pixel spacing 0.6 mm, voxel depth 0.6 mm, slice spacing 0.6 mm, slice thickness 1.2 mm, proton density water). The foot geometry was segmented in a custom segmentation software, MultiRigid [31]. The subject's plantar pressure data was recorded during normal gait at a self-selected walking on an emed plantar pressure machine (Novel, Munich, Germany). GRF data was collected by summing the plantar pressure results. Bone motion couldn't be measured *in vivo*, so BAREFOT bone motion results were compared to normative cadaveric data [3].

4.2.3 *Lattice Motivation & Implementation*

One drawback of 3D printing technology is that commercially available printer materials are not soft enough to accurately represent various tissue in the human body. In a previous study, we identified lattice microstructures as a means of recreating the non-linear elastic properties of plantar fat using stiff, elastically-linear printed material [32]. In the previous study we used simple

cubic lattice structures and identified a best-fit lattice to *in-vitro* fat measurements [23] (figure 4.1), but preliminary full body weight testing found the cubic lattice not robust to repeated testing.

Contrary to a cubic lattice, which has high stress concentrations at the intersections of columns, a Schoen gyroid lattice has much smother intersections and was found to be robust enough for repeated full body weight testing [26]. To optimize the gyroid lattice, we swept a portion of the gyroid lattice cell parameter space (unit cell size and volume percent fill), printing and testing different gyroid unit cells via compression testing to yield stress-strain curves. A gyroidal lattice microstructure with a unit cell size of 5 mm and 30 percent volumetric fill had elastic stress-strain properties that mimicked cadaveric plantar fat. While the stress-strain curve for this gyroid was vertically offset from that of plantar fat, the Young's modulus as a function of strain was similar, especially at the toe region (figure 4.2).

The STL surface mesh representing the soft tissue, previously exported from Solidworks, was imported into Simpleware +CAD (Synopsys). Using the Internal Structures Wizard tool, a Schoen gyroid unit cell with the previously determined properties was applied to the soft tissue, generating a new surface mesh. In this sense, a gyroid lattice microstructure was generated in the volume bounded by the soft tissue. The lattice structure was exported from +CAD as a surface mesh.

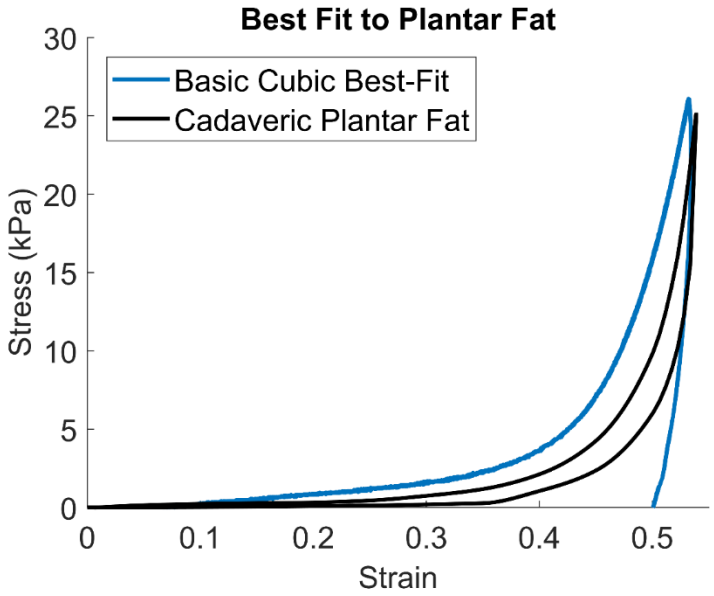

Figure 4.1. Best-fit lattice to plantar fat discovered in previous study [23], [32]. The lattice microstructure used simple cubic lattice cells, which provided a close fit, but were less durable than the gyroidal lattices used in the present study.

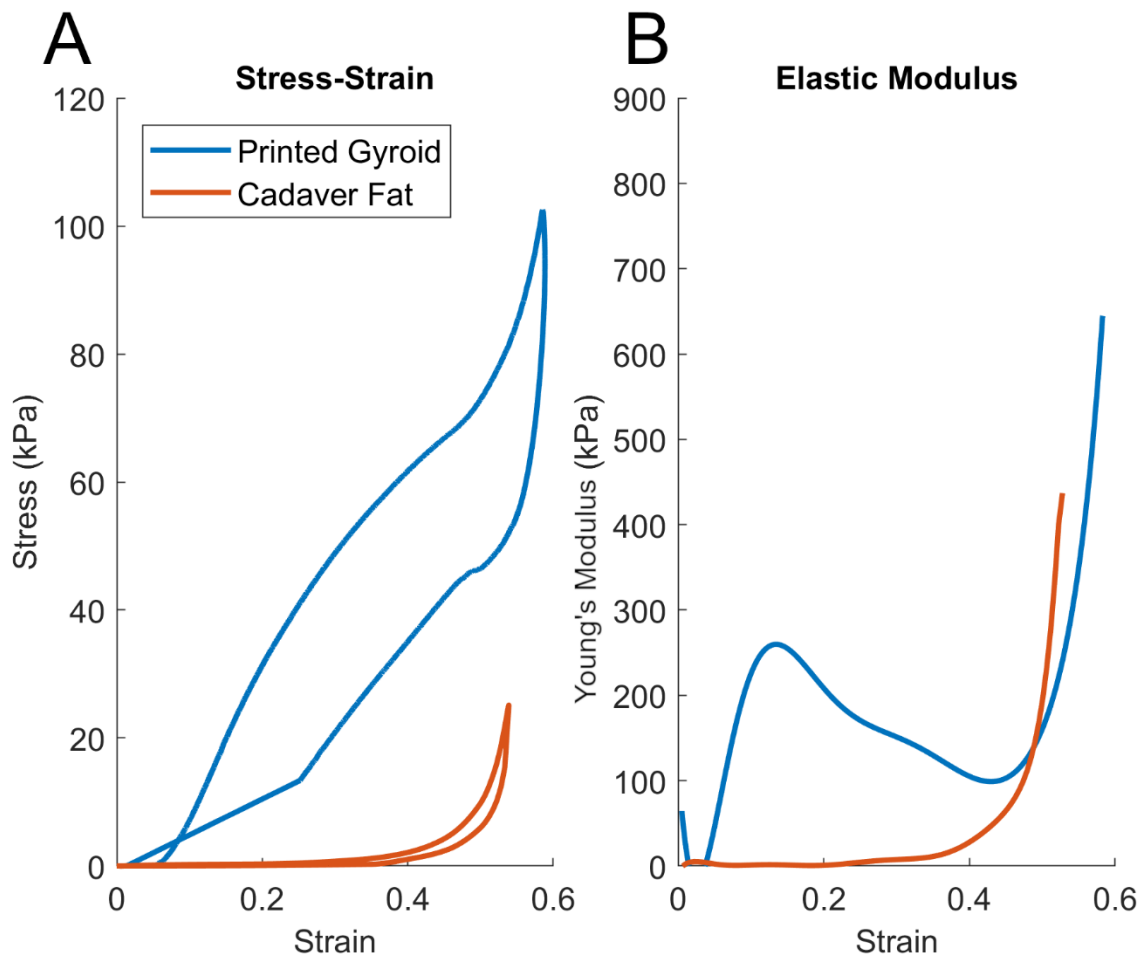

Figure 4.2. Compressive test results for best-fit gyroid lattice microstructure compared to that of cadaveric plantar fat. (A) Stress-strain curve for printed gyroid (blue) vs. cadaveric plantar fat (orange). (B) Elastic modulus for lattice vs. fat, which is the derivative of (A).

4.2.4 *Scan, Segment, and CAD*

The image stack from the CT scan was imported into MultiRigid for segmentation. Segmented regions consisting of bone, soft tissue, and skin were exported to STL, which were then imported into Meshlab (Autodesk, San Rafael, CA) for mesh cleaning and repairing. The cleaned surface meshes were then imported to Solidworks and converted to solid body geometries. To mimic the musculoskeletal system of the foot, including joint articulation and tendon actuation several key features were added to the BAREfoot in Solidworks. Tendon routing was defined, and tendon

sheathing was included to mimic the biological system and separate the tendon cords from the softer lattice microstructure (figure 4.3(B)). At key points in the tendon routing of significant directional change, stiff rings (Vero) were affixed to neighboring bones to serve the same purpose as retinacula (figure 4.3(B)). Without this pseudo-retinaculum, the tendon cords would tear the tendon sheathing and lattice soft tissue when placed under high tendon loads. To replicate the tight and minimal motion that occurs in the midfoot (talonavicular, naviculocuneiform, tarsometatarsal) and subtalar joints pseudo-ligaments were developed by filling the joint space with (FLX2070 (figure 4.3(A)). These pseudo-ligaments were designed to allow the midfoot bones to have the same range of motion during gait as the biological foot. The metatarsophalangeal (MTP) joints consisted of a soft hollow sphere encapsulating the joint to mimic the MTP joint capsule. The MTP joint space was left empty of printed material to allow for full biological range of motion. A 3mm thick offset geometry was added around the bones to give a soft (Tango) interface between the lattice structure (Tango) and skin material (Tango) (figure 4.3(C)). Holes were cut through the skin geometry to aid in support dissolution (figure 4.3(C)). To interface with the RGS, a large cylindrical extrusion was added to the positive y-axis of the talus (figure 4.3(B)). The Solidworks assembly was exported to STL.

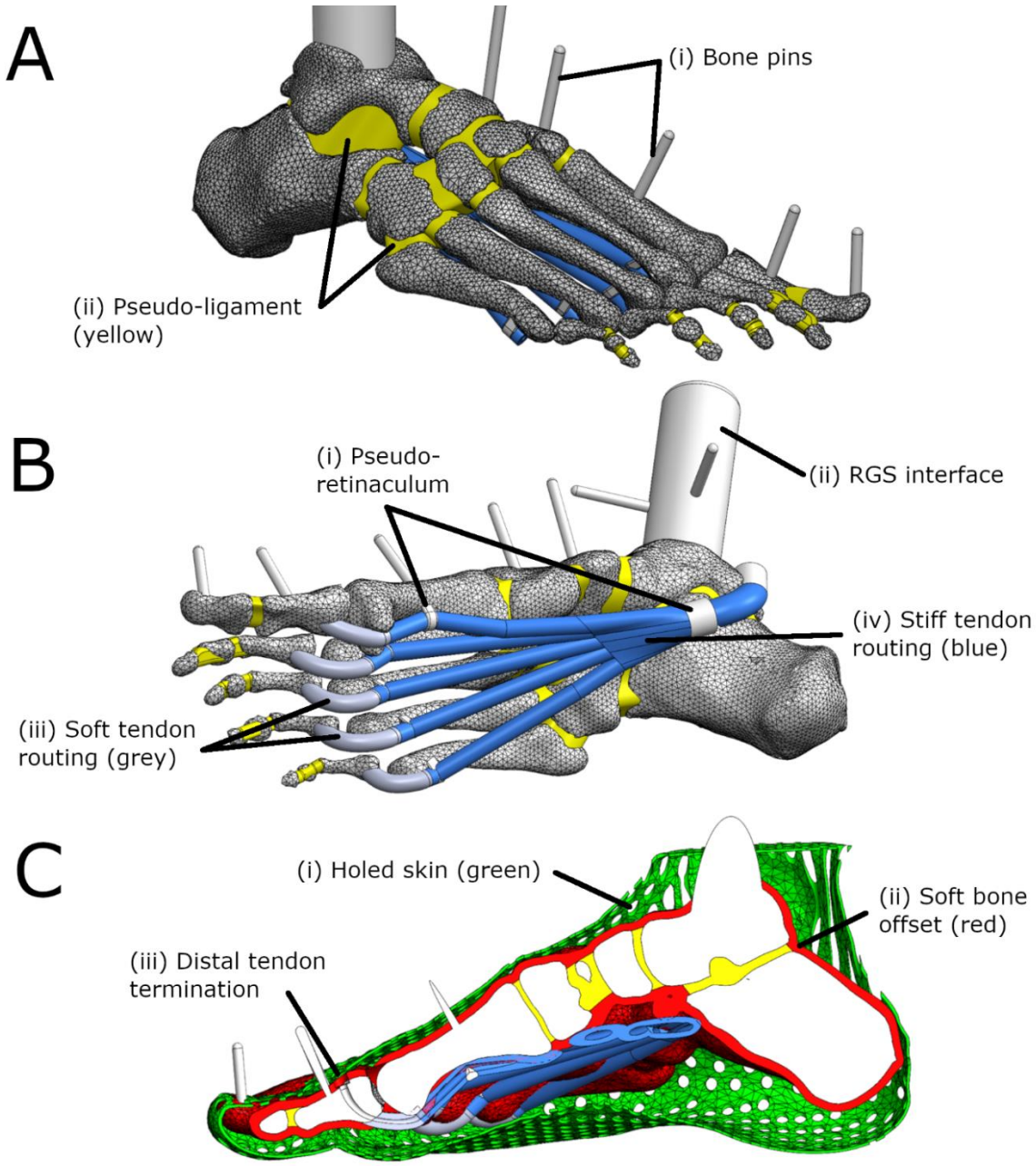

Figure 4.3. Solidworks assembly at various viewing angles. (A) Dorsal isometric view, excluding soft tissue. (i) Bone pins are used to measure relative bone angles. (ii) Pseudo-ligament is a Shore 70A material that was chosen to provide realistic midfoot flexion and constrain bone motion in the absence of anatomical ligaments. (B) Plantar isometric view, excluding soft tissue. (ii) Pseudo-retinaculum is made of stiff material (Tango) that constrain tendon motion at instances of gross axial change. Placement is *chosen to minimally* affect plantar pressure results. (ii) A 30mm diameter cylinder attaches to the talus along it's y-axis, and interfaces with a clamp on the RGS. (iii) This tendon routing is softer (Shore 60A) to minimize

its effect on plantar pressure data. (iv) Deep tendon routing that doesn't affect plantar pressure is maximally stiff (Vero) for strength considerations. (C) Sagittal, cross sectional view, including all components besides the lattice soft tissue *in* the empty space between (i) and (ii). (i) 1mm thick skin to strengthen latticed surface, with holes to aid in support dissolution. (ii) A soft material (Tango) offset 3mm from the bone surface. This offset provides a Tango to Tango interface between the lattice and bony geometry (Tango to Vero bonds are weaker). (iii) Proximal phalanges tendon insertion with the tendon cords knotted and the knots sitting in the countersunk holes.

4.2.5 *Printing and Post-Processing*

The lattice soft tissue file was joined with the exported STL assembly, taking the place of the original soft tissue mesh. The file set was then imported to Objet Studio, the print utility of the Objet350 Connex3, as an assembly and printed. The support material is soluble in a basic solution, so a 20 L aqueous solution with 2 percent sodium hydroxide and 1 percent sodium metasilicate by weight was prepared. The support cleaner was filled with the solution, the foot was submerged in the bath, and the cleaner was left running for about 15 hours to remove the support from the lattice voids. After the initial support dissolution, support had completely dissolved from everywhere in the foot except the tendon routing tubes, where it was then removed manually with a 5 Fr catheter. Tendon cords were then routed through their sheaths and terminated at their insertion points with knots (figure 4.4).

Figure 4.4. Photo of printed BAREFOOT model after support dissolution and tendon routing, ready to be tested on the RGS.

4.2.6 *Validation and Testing*

Articulation of the BAREFOOT was performed using the RGS, a 6-DOF robot with tendon force actuators capable of moving and loading the BAREFOOT in a manner that replicates *in vivo* kinematics and kinetics [3], [29]. The RGS is an inverse motion machine whereby the foot is rigidly mounted to a frame and the "ground" is moved with respect to the foot to recreate the relative foot-ground motion. The BAREFOOT model includes all bones including and distal to the talus, so there is no ankle joint or Achilles tendon. As part of a prior IRB approved study, normative 3-degree-of-freedom (3-DOF) tibial kinematics were recorded from 10 subjects performing four or five repeated gait trials in our motion analysis lab [3]. Using the normative *in vivo* 3-DOF tibia with respect to ground kinematics ($R_{TIB\ GND}$) and *in vitro* sagittal plane 1-DOF talus with respect

to tibia kinematics ($R_{TAL\,TIB}$) [3] 3-DOF talus with respect to ground kinematics ($R_{TAL\,GND}$) were calculated according to equation 1 and programmed into the robot.

$$R_{TAL\,GND} = R_{TAL\,TIB} R_{TIB\,GND} \tag{4.1}$$

In (4.1), $R_{TAL\,GND}$ is a 3x3 rotation matrix that describes the sagittal, frontal, and transverse plane rotation of the talus with respect to the ground as a function of the gait cycle. $R_{TAL\,TIB}$ and $R_{TIB\,GND}$ are similarly defined. Tendon forces, which were estimated from literature [33]–[36] using an EMG to force model with a 42 ms electromechanical delay [37] was used to apply force to the flexor hallucis longus and flexor digitorum longus tendons.

Because the printed materials composing the BAREFOOT model are only validated in terms of elasticity, we chose to evaluate the model using static trials. Dynamic trials are dependent on mass/density and strain-rate properties, which are not validated material properties in our model. Poses at 10, 30, 50, 70, and 90 percent stance were evaluated to be representative of stance phase, at 75 and 100 percent BW. Sagittal plane images for bone angle measurements were captured at 75 percent BW for comparison to a cadaveric study using the same load [3]. Plantar pressure results were recorded at 100 percent BW for comparison to the subject's *in vivo* data. The plantar pressure distributions and center of pressure (COP) trajectory for the BAREFOOT model and the subject's foot were compared qualitatively, and peak pressures under the metatarsal heads and hindfoot were compared quantitatively.

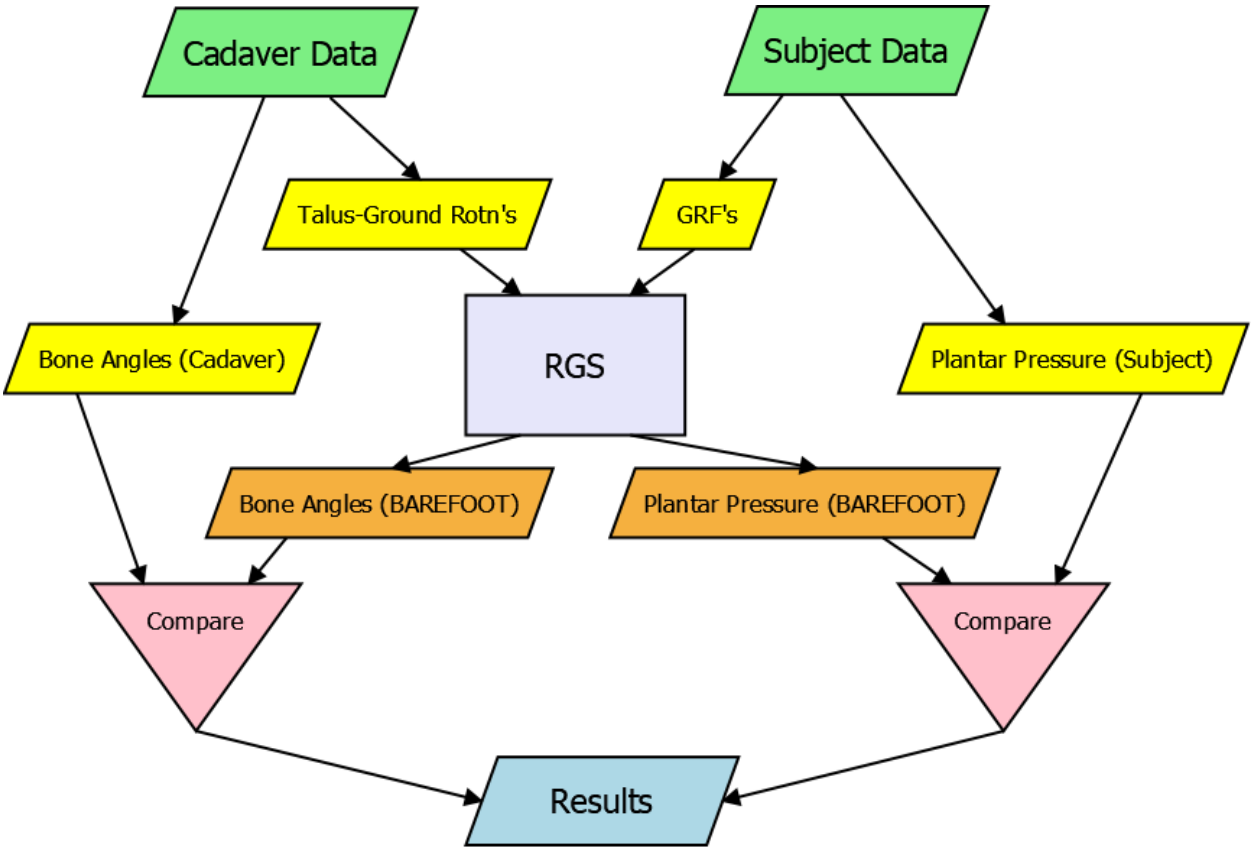

Figure 4.5. Flowchart showing RGS inputs, outputs, and validation methods.

4.3 Full Foot Results

Bone angle changes during gait for the BAREFOOT model agree closely with normative cadaver data (figure 4.6). As *in vivo,* the great toe joint (hallux to metatarsal) showed minimal motion during the first part of stand phase (0% to 75%) and then had large dorsiflexion in last stance. The total range of motion for the BAREFOOT hallux to metatarsal joint was 22.7 degrees compared to 59.0 for cadaveric feet. Unlike a biological foot, the BAREFOOT great toe returned to its neutral position at 100% gait, while the biological toe remains dorsiflexed at toe off.

Similar to the biological foot, the midfoot joints (navicular w.r.t. talus, cuneiform w.r.t. navicular and metatarsal w.r.t. cuneiform) had minimal motion. The BAREFOOT navicular w.r.t. talus joint range of motion was 6.3 degrees compared to 6.1 for cadaveric feet. A similarly close

match, the BAREFOOT cuneiform w.r.t. navicular joint range of motion was 12.5 degrees compared to 11.8 for cadaveric feet.

The angle plots are vertically offset to start at zero for both the BAREFOOT and subject data, as the BAREFOOT model yields accurate relative angles rather than absolute angles (figure 4.6) [3]. This zeroing was performed for sake of comparison. For the last 50 percent of stance, the cuneiform with respect to the navicular and first metatarsal with respect to talus are slightly more dorsiflexed in the BAREFOOT model than in the cadaver data (figure 4.6(A), (D)).

The BAREFOOT COP trajectory qualitatively matched key characteristics of the biological foot with the COP starting in the heel and then advancing forward towards the metatarsals in late stance. However, the BAREFOOT COP stayed in the hind and midfoot late into stance (figure 4.7). There was also a lateral shift in the BAREFOOT COP trajectory, and there was reduced pressure under the second and third toes as compared to the subject's *in vivo* plantar pressure profile, except for the first ray at 70 percent stance and the fourth and fifth ray at 90 percent stance (figure 4.7).

Peak pressures occurred under appropriate anatomical locations, e.g. the calcaneus and metatarsal heads, but with the BAREFOOT pressures overall being higher than the biological foot. For example, the distribution under the calcaneus in the BAREFOOT model consistently peaked at over twice the *in vivo* subject value in the BAREFOOT model (table 4.1). The pressures under the MTPs better matched the subject value and follow a similar trend of increase (170, 260, 300, 352.5, and 637.5 kPa for BAREFOOT respectively, and 65, 220, 360, 460, and 250 for the subject respectively (table 4.1).

Table 4.1. Regional peak pressure of BAREFOOT model compared to *in vivo* data from subject. Note that 637.5 is the max value that the emed pressure mat can read, and any BAREFOOT peak pressure of that value likely represents an oversaturated cell.

Percent Stance	Region	BAREFOOT Peak Pressure (kPa)	Subject Peak Pressure (kPa)
10	MTP's	170	65
	Hindfoot	637.5	260
30	MTP's	260	220
	Hindfoot	637.5	170
50	MTP's	300	360
	Hindfoot	637.5	305
70	MTP's	352.5	460
	Hindfoot	637.5	255
90	MTP's	637.5	250
	Hindfoot	0	0

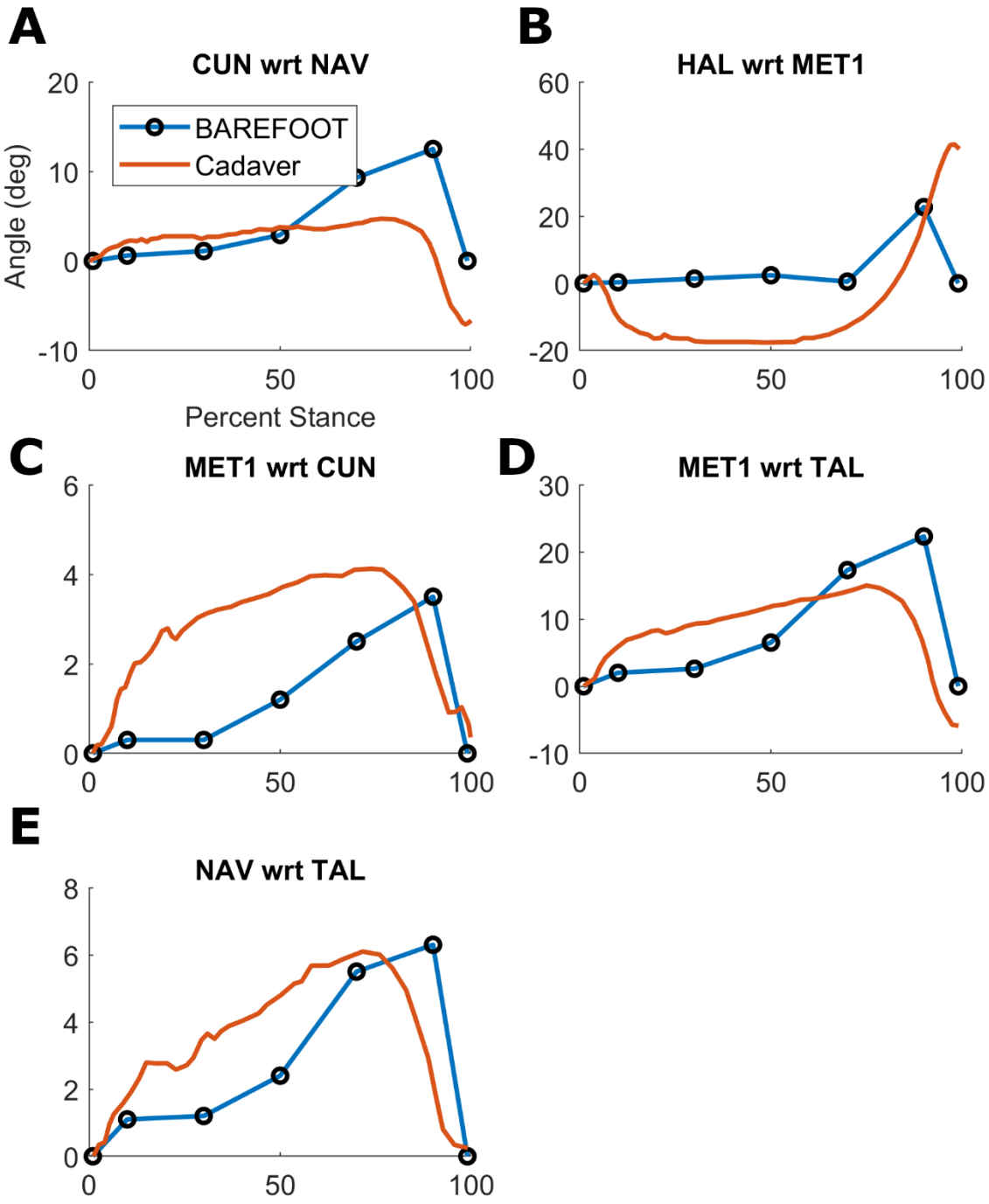

Figure 4.6. Relative bone angles along the first ray in the sagittal plane during stance, of the BAREFOOT model versus cadaveric data from literature. Positive angles represent dorsiflexion, and negative plantarflexion. All angles were normalized to start at 0, as our methods with the BAREFOOT model do not yield accurate absolute angles. (A) Cuneiform with respect to navicular. (B) Hallux (first ray proximal phalanx) with respect to the first metatarsal. (C) First

metatarsal with respect to medial cuneiform. (D) First metatarsal with respect to talus. (E) Navicular with respect to talus.

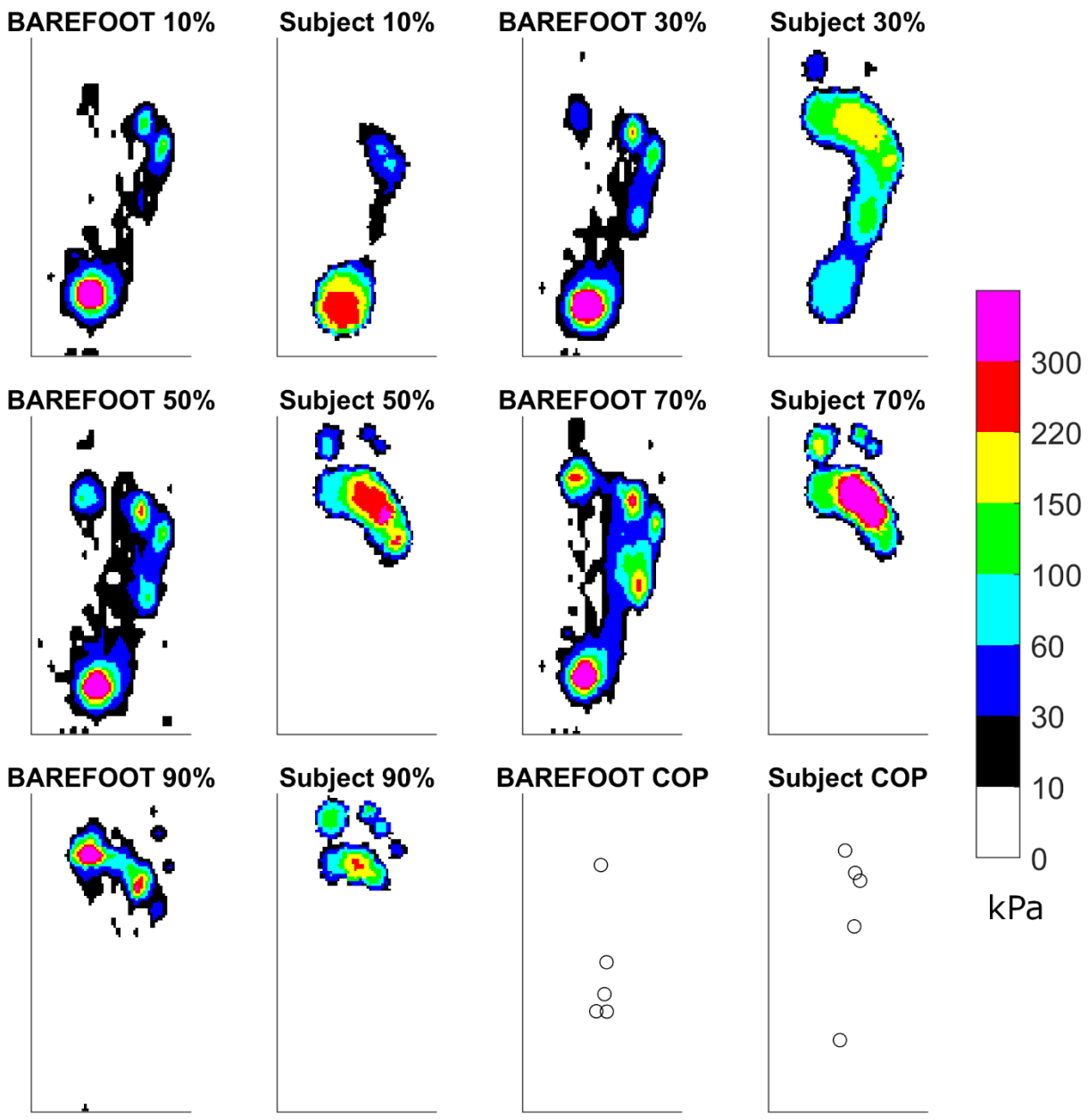

Figure 4.7. Plantar pressure distributions for BAREFOOT on the RGS versus *in vivo* subject data during normal gait, at 10, 30, 50, 70, and 90 percent of stance phase. Also included are plots of the center of pressure (COP) trajectory at these same percent stance values.

4.4 Full Foot Discussion

In this paper we leveraged medical imaging, 3D printing and lattice microstructures to create a biomimetic physical model of the human foot. We envision the BAREFOOT model will be used in the future to study novel orthopedic surgical interventions for various foot pathologies. The BAREFOOT model featured soft tissue with a realistic elastic profile and highly accurate, subject specific bony geometry.

In general, the relative bone angles agreed closely with the cadaver results (figure 4.6). For the cases in which significant deviations did occur, it's possible this was caused by issues with foot rotation relative to the ground plate, tendon forces, and uniform soft tissue (figure 4.6(A), (B), (D)). However, the success of these results shows that the non-anatomical ligaments used to constrain bone motion were adequate, and that generating a more realistic ligament network isn't necessary.

There are a variety of likely reasons for the differences between plantar pressure of the BAREFOOT model and the subject. All the soft tissue in the foot is approximated with a single lattice microstructure. In the biological foot there are other soft tissues, notably muscle, that are lacking representation in the BAREFOOT model. Furthermore, even plantar fat itself varies in stiffness regionally in the foot, but we are matching to averaged data [23]. The high peak pressures in the subcalcaneal region were a result of the lattice fully compressing into a thin layer, and the stiff bony material of the printed calcaneus pressing directly onto the mat (figure 4.7). A biomechanically accurate regional variation in lattice stiffness would yield more accurate plantar pressure results, which we know anecdotally from previous attempts.

Another cause of the differing pressure results could be rotation data used to program the RGS. The data used to generate these rotations was a) sourced from a cadaver study and thus not

subject specific and b) only created with sagittal plane angles. Furthermore, even if these generated rotations were perfect, they were applied to a talus coordinate system which is difficult to construct in a repeatable manner. The same steps for defining the talus coordinate system were used in this study as in the cadaver study, but they were placed based on 2D projections of a 3D bone [3]. Thus, it is unlikely that the embedded talus coordinate system of the BAREFOOT model was equal to that of the taluses in the cadaver study.

The last issue with the plantar pressure results is that the second and third toe had reduced pressure as compared to the *in vivo* data (figure 4.7). Besides the discussed error in RGS rotations causing this, the tendon forces used to generate forces under the phalanges via the flexor hallicus longus and flexor digitorum longus were borrowed from a normative cadaver dataset and weren't subject specific. It's possible that the subject's *in vivo* tendon forces were considerably larger.

Chapter 5. CONCLUSION AND FUTURE WORK

5.1 LATTICE STUDY

We presented a framework for reducing the elasticity of 3D printed materials and creating nonlinear elastic profiles from linearly elastic base materials. The elasticity was lowered through the creation of lattice microstructures in the material. The effects of varying the properties of the elastic microstructure were empirically quantified with respect to five explored variables: element diameter, element spacing, element cross-sectional geometry, element arrangement, and lattice rotation (figure 2.2). In doing so, we achieved one specific lattice microstructure that had a stress-strain curve closely fitting that of cadaveric plantar fat (figure 2.4(F)). We also determined that element diameter and element spacing are the most important lattice properties for tuning the stress-strain magnitude, while lattice rotation is important in tuning linearity.

The purpose for this work was to fulfill a missing piece of current efforts to create 3D printed physical models of biological systems for the study of biomechanics and inform similar future efforts. Currently, commercially available 3D printing materials all have elastic profiles that are far too stiff and linear to accurately represent human soft tissue. By directly printing a metamaterial representative of soft tissue, we have removed the need for casting techniques that are largely used to address this elasticity issue. Additionally, we have provided a framework for tuning the elastic profile of any 3D printed material through implementing lattice microstructures.

Future work will involve applying the techniques developed here to the printing of biomechanical testbeds. Physical, real-world biomechanical testbeds have the potential to transform the study of biomechanics similarly to computer simulations, offering different and complementary capabilities. Our group has already begun the preliminary stages of applying the

best-fit lattice discovered here to a foot model for investigations into intra-joint pressures found in great toe arthritis. We anticipate that using these microstructures to represent plantar fat in our model will increase the realism and accuracy of observed quantities.

5.2 FULL FOOT BAREFOOT MODEL

In this study, we designed and manufactured a biomechanically and anatomically realistic foot model (BAREFOOT). BAREFOOT is entirely 3D printed with minimal post processing and utilizes previously validated soft tissue lattice microstructures [32]. The model includes all bones including and distal to the talus and features a functional flexor hallucis longus and flexor digitorum longus. The BAREFOOT model was evaluated at five representative poses during stance phase on a robotic gait simulator (RGS) at 75 and 100 percent bodyweight (BW). The 75 percent BW trials were used to capture bone angle motion for comparison to a cadaver study performed at the same loads, and the 100 percent BW trials were used to capture plantar pressure distributions.

We have developed an existence proof of a full foot BAREFOT model and have successfully validated the plantar fat properties and bone motion. Future work will include validating other aspects of the model and working towards improving the plantar pressure results. We have shown that this model is stronger than a cadaver, and that highly accurate geometries of any scannable foot pathology are printable in fine resolution.

BIBLIOGRAPHY

[1] J. P. Kostuik and T. J. Smith, "Pitfalls of biomechanical testing," *Spine (Phila. Pa. 1976).*, vol. 16, no. 10, pp. 1233–5, 1991.

[2] K. Narioka, S. Moriyama, and K. Hosoda, "Development of Infant Robot with Musculoskeletal and Skin System," no. January 2015, pp. 1–4.

[3] E. C. Whittaker, P. M. Aubin, and W. R. Ledoux, "Foot bone kinematics as measured in a cadaveric robotic gait simulator," *Gait Posture*, vol. 33, no. 4, pp. 645–650, 2011.

[4] R. Eisma and T. Wilkinson, "From 'Silent Teachers' to Models," *PLoS Biol.*, vol. 12, no. 10, pp. 1–5, 2014.

[5] D. L. A. Camacho, W. R. Ledoux, E. S. Rohr, B. J. Sangeorzan, and R. P. Ching, "A three-dimensional, anatomically detailed foot model: A foundation for a finite element simulation and means of quantifying foot-bone position," *J. Rehabil. Res. Dev.*, vol. 39, no. 3, pp. 401–409, 2002.

[6] M. Vande Weghe, M. Rogers, M. Weissert, and Y. Matsuoka, "The ACT Hand: design of the skeletal structure," *IEEE Int. Conf. Robot. Autom.*, vol. 4, no. April, pp. 3375–3379, 2004.

[7] R. Balasubramanian and Y. Matsuoka, "Biological Stiffness Control Strategies for the Anatomically Correct Testbed (ACT) Hand," *IEEE Int. Conf. Robot. Autom.*, pp. 737–742, 2008.

[8] E. Rombokas, E. Theodorou, M. Malhotra, E. Todorov, and Y. Matsuoka, "Tendon-Driven Control of Biomechanical and Robotic Systems: A Path Integral Reinforcement Learning Approach.," *IEEE Int. Conf. Robot. Autom.*, 2012.

[9] B. L. Tai *et al.*, "Development of a 3D-printed external ventricular drain placement simulator: technical note," *J Neurosurg*, vol. 123, no. October, pp. 1070–1076, 2015.

[10] T. Mashiko, T. Konno, N. Kaneko, and E. Watanabe, "Training in Brain Retraction Using a Self-Made Three-Dimensional Model," *World Neurosurg.*, vol. 84, no. 2, pp. 585–590, 2015.

[11] H. a Mansy, J. R. Grahe, and R. H. Sandler, "Elastic properties of synthetic materials for soft tissue modeling.," *Phys. Med. Biol.*, vol. 53, pp. 2115–2130, 2008.

[12] F. Duboeuf, A. Basarab, H. Liebgott, E. Brusseau, P. Delachartre, and D. Vray, "Investigation of PVA cryogel Young's modulus stability with time, controlled by a simple reliable technique.," *Med. Phys.*, vol. 36, no. 2, pp. 656–661, 2009.

[13] Stratasys, "PolyJet Materials Data Sheet." 2015.

[14] V. Narayanan *et al.*, “Endoscopic skull base training using 3D printed models with pre-existing pathology,” *Eur. Arch. Oto-Rhino-Laryngology*, vol. 272, no. 3, pp. 753–757, 2015.

[15] B. L. Tai *et al.*, “A physical simulator for endoscopic endonasal drilling techniques: technical note.,” *J. Neurosurg.*, vol. 124, no. March, pp. 1–6, 2015.

[16] A. G. Kolpakov, “Determination of the average characteristics of elastic frameworks,” *J. Appl. Math. Mech.*, vol. 49, no. 6, pp. 739–745, 1985.

[17] P. S. Theocaris, G. E. Stavroulakis, and P. D. Panagiotopoulos, “Negative Poisson’s ratios in composites with star-shaped inclusions: a numerical homogenization approach,” *Arch. Appl. Mech.*, vol. 67, no. 4, pp. 274–286, 1997.

[18] G. E. Stavroulakis, “Auxetic behaviour: Appearance and engineering applications,” *Phys. Status Solidi Basic Res.*, vol. 242, no. 3, pp. 710–720, 2005.

[19] Z. Qian *et al.*, “Quantitative Prediction of Paravalvular Leak in Transcatheter Aortic Valve Replacement Based on Tissue-Mimicking 3D Printing,” *JACC: Cardiovascular Imaging*, vol. 10, no. 7. pp. 719–731, 2017.

[20] D. Maragiannis, M. S. Jackson, S. R. Igo, S. M. Chang, W. A. Zoghbi, and S. H. Little, “Functional 3D Printed Patient-Specific Modeling of Severe Aortic Stenosis,” *Journal of the American College of Cardiology*, vol. 64, no. 10. pp. 1066–1068, 2014.

[21] K. Wang, C. Wu, Z. Qian, C. Zhang, B. Wang, and M. A. Vannan, “Dual-material 3D printed metamaterials with tunable mechanical properties for patient-specific tissue-mimicking phantoms,” *Addit. Manuf.*, vol. 12, pp. 31–37, 2016.

[22] K. Wang *et al.*, “Controlling the mechanical behavior of dual-material 3D printed meta-materials for patient-specific tissue-mimicking phantoms,” *Mater. Des.*, vol. 90, pp. 704–712, 2016.

[23] S. Pai and William R. Ledoux, “The compressive mechanical properties of diabetic and non- diabetic plantar soft tissue,” *J. Biomech.*, vol. 43, no. 9, pp. 1754–1760, 2010.

[24] P. Macioce, “Viscoelastic Damping,” *Sound Vib.*, pp. 4–5, 2003.

[25] C. Schumacher, B. Bickel, J. Rys, S. Marschner, C. Daraio, and M. Gross, “Microstructures to control elasticity in 3D printing,” *ACM Trans. Graph.*, vol. 34, no. 4, p. 136:1-136:13, 2015.

[26] A. H. Schoen, “Infinite periodic minimal surfaces without self-intersections,” *Nasa Tech. Note D-5541*, p. 92, 1970.

[27] C. Yan, L. Hao, A. Hussein, and D. Raymont, “Evaluations of cellular lattice structures manufactured using selective laser melting,” *Int. J. Mach. Tools Manuf.*, vol. 62, pp. 32–38, 2012.

[28] P. H. U. Kim, X. Chen, H. Hillstrom, S. J. Ellis, J. R. Baxter, and J. T. Deland, “Moberg osteotomy shifts contact pressure plantarly in the first metatarsophalangeal joint in a biomechanical model,” *Foot Ankle Int.*, vol. 37, no. 1, pp. 96–101, 2016.

[29] P. M. Aubin, E. Whittaker, and W. R. Ledoux, “A robotic cadaveric gait simulator with fuzzy logic vertical ground reaction force control,” *IEEE Trans. Robot.*, vol. 28, no. 1, pp. 246–255, 2012.

[30] V. Isvilanonda and W. R. Ledoux, “Finite Element Modeling of the Foot,” *ProQuest Diss. Theses*, p. 233, 2015.

[31] Y. Hu, W. R. Ledoux, M. Fassbind, E. S. Rohr, B. J. Sangeorzan, and D. Haynor, “Multi-Rigid Image Segmentation and Registration for the Analysis of Joint Motion From Three-Dimensional Magnetic Resonance Imaging,” *J. Biomech. Eng.*, vol. 133, no. 10, p. 101005, 2011.

[32] L. K. Johnson, C. Richburg, M. Lew, P. M. Aubin, W. R. Ledoux, and E. Rombokas, “3D printed lattice microstructures to mimic soft biological materials,” *IOP B&B*, pp. 1–12.

[33] T. L. Wickiewicz, R. R. Roy, P. L. Powell, and V. R. Edgerton, “Muscle architecture of the human lower limb.,” *Clinical Orthopaedics and Related Research*, no. 179. pp. 275–83, 1983.

[34] M. R. Pierrynowski and J. B. Morrison, “A physiological model for the evaluation of muscular forces in human locomotion: theoretical aspects,” *Math. Biosci.*, vol. 75, no. 1, pp. 69–101, 1985.

[35] T. Fukunaga, R. R. Roy, F. G. Shellock, J. A. Hodgson, and V. R. Edgerton, “Specific tension of human plantar flexors and dorsiflexors.,” *J. Appl. Physiol.*, vol. 80, no. 1, pp. 158–65, 1996.

[36] J. Perry, *GAIT Pathological Function*. 1992.

[37] S. Zhou, D. L. Lawson, W. E. Morrison, and I. Fairweather, “Electromechanical delay in isometric muscle contractions evoked by voluntary, reflex and electrical stimulation,” *Eur. J. Appl. Physiol. Occup. Physiol.*, vol. 70, no. 2, pp. 138–145, 1995.